



Article

Flood Detection Using Multiple Chinese Satellite Datasets during 2020 China Summer Floods

Lianchong Zhang ^{1,†} and Junshi Xia ^{2,*,†,‡}

¹ Aerospace Information Research Institute, Chinese Academy of Sciences, Beijing 100094, China; zhanglc@aircas.ac.cn

² Geoinformatics Unit, RIKEN Center for Advanced Intelligence Project (AIP), Tokyo 103-0027, Japan

* Correspondence: junshi.xia@riken.jp; Tel.: +81-070-4382-6049

† These authors contributed equally to this work.

‡ Current address: Nihonbashi 1-Chome Mitsui Building, 15th Floor, 1-4-1 Nihonbashi, Chuo-ku, Tokyo 103-0027, Japan.

Abstract: Multiple source satellite datasets, including the Gaofen (GF) series and Zhuhai-1 hyperspectral, are provided to detect and monitor the floods. Considering the complexity of land cover changes within the flooded areas and the different characteristics of the multi-source remote sensing dataset, we proposed a new coarse-to-fine framework for detecting floods at a large scale. Firstly, the coarse results of the water body were generated by the binary segmentation of GF-3 SAR, the water indexes of GF-1/6 multispectral, and Zhuhai-1 hyperspectral images. Secondly, the fine results were achieved by the deep neural networks with noisy-label learning. More specifically, the Unet with the T-revision is adopted as the noisy label learning method. The results demonstrated the reliability and accuracy of water mapping retrieved by the noisy learning method. Finally, the differences in flooding patterns in different regions were also revealed. We presented examples of Poyang Lake to show the results of our framework. The rapid and robust flood monitoring method proposed is of great practical significance to the dynamic monitoring of flood situations and the quantitative assessment of flood disasters based on multiple Chinese satellite datasets.

Keywords: flood mapping; multiple-source; Chinese satellites; summer flood



Citation: Zhang, L.; Xia, J. Flood Detection Using Multiple Chinese Satellite Datasets during 2020 China Summer Floods. *Remote Sens.* **2022**, *14*, 51. <https://doi.org/10.3390/rs14010051>

Academic Editors: Chunxiang Cao and Min Xu

Received: 17 November 2021

Accepted: 20 December 2021

Published: 23 December 2021

Publisher's Note: MDPI stays neutral with regard to jurisdictional claims in published maps and institutional affiliations.



Copyright: © 2021 by the authors. Licensee MDPI, Basel, Switzerland. This article is an open access article distributed under the terms and conditions of the Creative Commons Attribution (CC BY) license (<https://creativecommons.org/licenses/by/4.0/>).

1. Introduction

Floods are the most dangerous, common, and serious natural calamity, causing more mortality and property damage than other disasters [1–3]. According to the 2019 World Risk Report, flood disasters were the worst form of disaster, accounting for almost 5000 deaths in 2019 and 4913 deaths between 2009 and 2018 (<https://reliefweb.int/report/world/natural-disasters-2019> (accessed on 30 June 2019)). It also caused a substantial economic loss (36.8 billion US dollars in 2019) and affected 60 million people worldwide. In 2020, the Asian summer monsoon's low-pressure systems were powerful and stable, allowing more water vapor to flow from the Indian and Pacific oceans to South and East Asia [4]. From June 2020, rainfall had caused floods and landslides that had impacted millions of people across South and East Asia. The severe floods happened in China, India, and the west regions of Japan [5].

From June 2020, China's most severely damaged areas occurred around the Yangtze River, Huai River, and their tributaries. The Yangtze River's upper and middle basins and its tributaries were flooded in June, affecting 14 million people in numerous provinces, including Sichuan, Hubei, and Hunan. With more rain in July, floods started to extend to lower regions of the Yangtze basin, such as Jiangxi, Anhui, and Jiangsu. According to the Chinese Ministry of Emergency Management, by the end of July, flooding had displaced 40 million people across 27 provinces with more than 200 people missing or dead and 500,000 buildings destroyed or damaged [6].

Due to the exponential growth of remote sensors, several satellites were deployed to provide vast land coverage data for disaster monitoring and damage assessment [7,8]. These satellites can provide optical and synthetic aperture radar (SAR) images. Optical image detection is straightforward to investigate since it has similar properties to visual perception. Considering the spatial and temporal resolutions, free available Landsat-8 and Sentinel-2 are good choices [9,10]. The main disadvantage of optical is that they cannot obtain images when meeting the bad weather conditions (e.g., clouds) in the affected areas. Unlike optical sensors, SAR sensors are active sensors that work throughout every environment and at any time of day, enabling monitoring disasters by rain and cloud. China has constructed, launched, and operated many series of high-resolution spacecraft independently over the last decade, notably the GaoFen (GF) series, which include both optical and SAR satellites [11]. Many new companies, such as Chang Guang Satellite Technology Co., Ltd., Changchun, China, have developed in the area of commercial satellite research, satellite development, and utilization [12]. During the flooding periods, both the GF series and the commercial satellites provide many images to support the flood mapping.

Flood detection technologies have been intensively examined in recent decades based on optical and SAR pictures in varying resolutions [13–15]. Typical approaches to map flood inundation include: (1) extract the water bodies from pre-disaster and post-disaster images and then detect the changes [16–18]; (2) directly identify pixel-wise or object-wise changes from the pre-disaster and post-disaster images [19,20]. The highly absorptive capacities of water in short wave infrared spectrum (SWIR) and near-infrared (NIR) spectrum and their combinations (resulting in normalized difference water index, NDWI) are exploited in the optical images [21,22]. However, optical imagery cannot split water and cloud shadows with low SWIR and NIR reflectance values. In SAR images, the water is easily identified because of lower backscatter values than other classes. Inundated vegetation and floods in metropolitan areas may generate an increase in backscatter during flooding because of a “double bounce” effect [23].

Deep learning and computer vision advances are already having a substantial impact on the current status of remote sensing [24,25]. Deep learning techniques, particularly convolutional neural networks (CNN), are even more accurate in categorizing land cover and image scene since 2015, and their application has increased significantly [26]. Most approaches, however, are used for urban and vegetated coverage. Very few studies are paid attention to water detection, in particular for flood mapping [27]. For instance, Li et al. [28] developed active self-learning CNNs based on the intensity and coherence of TerraSAR-X for mapping the urban flood. Rahnemoonfar et al. [29] combined densely connected CNN and RNN to detect the floods using UAV images. In [30], the pre-disaster and post-disaster Sentinel-1/2 and post-disaster VHR optical datasets are fused with the CNN to predict the high-resolution flood mapping result. Then, large-scale Sentinel-1/2 flooding datasets, such as Sen1Floods11, are presented to aid in the operationalization of deep learning methods [31].

In this paper, we proposed a new coarse-to-fine framework for detecting floods at a large scale. Firstly, the coarse results of the water body were generated by the binary segmentation of GF-3 SAR, the water indexes of GF-1/6 multispectral, and Zhuhai-1 hyperspectral images. Secondly, the fine results were achieved by the deep neural networks with noisy-label learning. The U-net with the T-revision [32] is adopted as the noisy label learning method. This study is of particular importance because the performance of deep learning techniques for flood detection is verified in multi-source Chinese datasets, including multispectral (GF-1 and GF-6), hyperspectral (Zhuhai-1), and SAR (GF-3) images. Another contribution of this paper is to use noisy label learning to improve the performance of flood detection.

2. Study Area and Datasets

2.1. Study Area

The middle and lower reaches of the Yangtze River (shown in Figure 1) are located to the north of the Nanling Mountains, south of the Huai River in the Qinling Mountains,

east to the East China Sea and the Yellow Sea, and west to Wushan. The administrative divisions include Hubei, Hunan, Jiangxi, Anhui, Jiangsu, Zhejiang, and Shanghai, with spans $108^{\circ}22' 123^{\circ}10'E$ and $24^{\circ}29' 35^{\circ}20'N$. There are various types of landforms in the region, including plains, such as the Yangtze River Delta Plain, as well as mountains such as Dabie Mountain, Xuefeng Mountain, and Luoxiao Mountain. The mountains are interspersed with vast hills and basins. The Yangtze, Huai, Xiang, Han and Gan rivers with an average annual runoff of more than 50 billion cubic meters are distributed. The five major lakes in China Poyang Lake, Dongting Lake, Taihu Lake, and Hongze Lake are also located in the regions of The Yangtze, Huai, Xiang, Han and Gan rivers. From June to July 2020, extreme rainfall and climate events occurred in the middle and lower reaches of the Yangtze River. Heavy rain warnings were issued for 41 consecutive days. The precipitation in the basin reached 410.4 mm, an increase of 45.3% over the same period of the previous year. Rivers and lakes continued to exceed the historical water level.

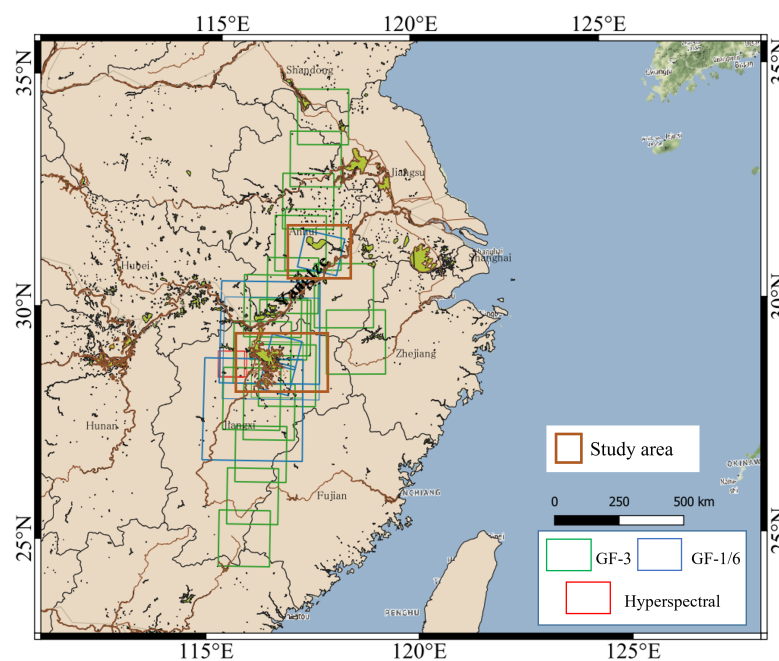


Figure 1. Study area and used datasets in this work.

2.2. Datasets

In this work, we mainly used the multispectral (GF-1 and GF-6), SAR (GF-3), and Hyperspectral (Zhuhai-1) images as the data source of post-disaster. China High-resolution Earth Observation System (CHEOS), which consists of seven optical/microwave satellites (refer to GaoFen, GF), was approved by the Chinese government in 2010. The cameras used in GF-1 include two 2 m Pan/8 m MS cameras and four 16 m MS medium-resolution and wide-field cameras. GF-3 can obtain full-polarization, dual-polarization, and single-polarization imagery with the imaging bandwidth of 5–650 km and a resolution of 1–500 m. GF-6 is equipped with one 2 m panchromatic/8 m MS camera and one 16 m MS medium-resolution and wide-view camera. GF series are competent for many applications such as flood mapping. The Zhuhai-1 Hyperspectral satellite has been launched and managed by Zhuhai Orbita Aerospace Science and Technology Co., Ltd., as a commercial remote sensing microsatellite constellation. The Zhuhai-1 Hyperspectral datasets we used include 32 bands with a resolution of 10 m. The main parameters of GF-1/6, GF-3, and Zhuhai-1 hyperspectral are given in Table 1. The used spectral bands of GF-1/6 and Zhuhai-1 hyperspectral are listed in Table 2.

Table 1. The primary characteristics of the Remote-Sensing products employed in this study.

Satellite	Date	Mode	Bands	Lat/Lon	Spatial Resolution (m)
GF-3	2020-7-9	Dual-Polarization	HH, HV	118.2E/30.4N	5
GF-3	2020-7-9	Dual-Polarization	HH, HV	118.5E/29.4N	5
GF-3	2020-7-11	Dual-Polarization	HH, HV	115.8E/25.2N	5
GF-3	2020-7-11	Dual-Polarization	HH, HV	116.0E/26.1N	5
GF-3	2020-7-11	Dual-Polarization	HH, HV	116.2E/27.0N	5
GF-3	2020-7-11	Dual-Polarization	HH, HV	116.4E/27.9N	5
GF-3	2020-7-11	Dual-Polarization	HH, HV	116.6E/28.8N	5
GF-3	2020-7-11	Dual-Polarization	HH, HV	116.8E/29.7N	5
GF-3	2020-7-11	Dual-Polarization	HH, HV	116.9E/30.6N	5
GF-3	2020-7-11	Dual-Polarization	HH, HV	117.1E/31.6N	5
GF-3	2020-7-11	Dual-Polarization	HH, HV	117.3E/32.5N	5
GF-3	2020-7-11	Dual-Polarization	HH, HV	117.5E/33.4N	5
GF-3	2020-7-11	Dual-Polarization	HH, HV	117.7E/34.3N	5
GF-3	2020-7-13	Dual-Polarization	HH, HV	116.6E/29.7N	5
GF-3	2020-7-13	Dual-Polarization	HH, HV	116.9E/28.7N	5
GF-3	2020-7-13	Dual-Polarization	HH, HV	115.9E/28.2N	5
GF-3	2020-7-13	Dual-Polarization	HH, HV	116.2E/29.4N	5
GF-3	2020-7-13	Dual-Polarization	HH, HV	116.4E/30.2N	5
GF-3	2020-7-25	Dual-Polarization	HH, HV	117.5E/31.6N	5
GF-1	2020-2-18	Wide Field of View (WFV)	4 bands	116.0E/27.9N	16
GF-1	2020-2-18	Wide Field of View (WFV)	4 bands	116.4E/29.6N	16
GF-1	2020-6-16	Wide Field of View (WFV)	4 bands	116.5E/29.3N	16
GF-1	2020-4-16	Wide Field of View (WFV)	4 bands	116.5E/28.9N	16
GF-1D	2020-7-25	Panchromatic and multispectral (PMS)	4 bands	116.6E/28.5N	8
GF-1D	2020-7-25	Panchromatic and multispectral (PMS)	4 bands	116.7E/29.1N	8
GF-6	2020-7-25	Panchromatic and multispectral (PMS)	4 bands	117.7E/31.3N	8
Zhuhai-1	2020-3-15	Hyperspectral	32 bands	115.5E/28.8N	10
Zhuhai-1	2020-7-17	Hyperspectral	32 bands	115.5E/28.8N	10

Table 2. The spectral bands of GF-1, GF-1D, GF-6 and Zhuhai-1 hyperspectral used in this study.

Satellite	Model	Bands
GF-1	WFV/PMS	B1: 450–520 nm, B2: 520–590 nm, B3: 630–690 nm, B4: 770–890 nm
GF-6	PMS	B1: 450–520 nm, B2: 520–600 nm, B3: 630–690 nm, B4: 760–900 nm
Zhuhai-1	Hyperspectral	400–1000 nm (32 bands with spectral resolution of 2.5 nm)

3. Methods

Multiple source datasets, especially post-flood SAR images, are obtained when the flood happens. If the pre-flood and post-flood images have different spectral and spatial characteristics or from various sensors (e.g., GF-1 and GF-3), the traditional change detection may fail to produce accurate flood mapping. However, the coarse water extraction or flood detection result can be easily obtained from different source images. We need to consider an effective way to produce better performance flood detection results based on the coarse results. In order to alleviate this problem, this paper proposes a coarse-to-fine flood detection based on noisy label learning. The main content includes image preprocessing, coarse flood extraction, fine flood extraction based on deep learning, and noisy-label learning. The overall technical process is shown in Figure 2. In the image preprocessing stage, for the optical datasets, radiation calibration and atmospheric correction are applied. For both optical and SAR datasets, we apply the image filter to remove the speckle noise.

In the coarse flood extraction stage, we extract the water bodies from pre-flood and post-flood datasets. For different sensors types, we use different methods. For instance, for the GF-3 SAR images, we define the combinations of threshold to separate the water from backscattering. For the optical images, such as GF-1/6 and Zhuhai-1 hyperspectral, we use the different water indices to extract the water. Then, the coarse flood map is obtained from the difference between the pre-flood and post-flood water results. In the stage of fine flood extraction, we stacked the features from pre-flood and post-flood datasets and adopted the coarse flood mapping results obtained from the previous stage as the training set. The noisy-label learning technique is used to redefine and improve classification performance.

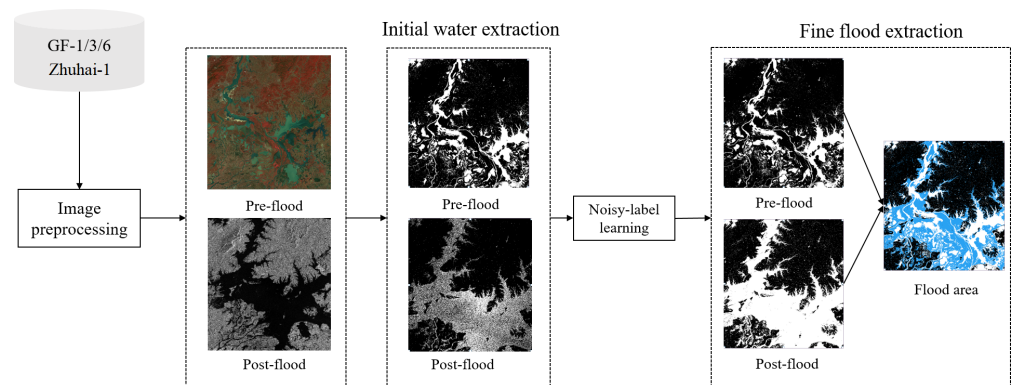


Figure 2. The main flowchart of flood detection.

3.1. Image Preprocessing

We used the GF-1/6 L1A, GF-3 L2, and Zhuhai-1 hyperspectral L1B datasets in this work. For the GF-1/6, we adopted radiation calibration and atmospheric correction, which is based on 6S (Second Simulation of a Satellite Signal in the Solar Spectrum) model, in the PIE software for the preprocessing. For more details of PIE software, please refer to the official website (<https://www.piesat.cn/en/index.html>) (accessed on 2 August 2021). GF-3 L2 and Zhuhai-1 hyperspectral L1B datasets are already preprocessed after relative radiation correction and system-level geometric correction by the data provider. Furthermore, a median filter (window size: 3×3) is used to reduce the noise of all images.

3.2. Coarse Flood Extraction

For GF-3 SAR, the cross-polarized band mainly reflects the volume scattering information, which is less sensitive to specular reflection. Due to the smooth surface and homogeneity of the water body, the noise level in the cross-polarized image is low, and the intra-class variance is slight. Compared with the same-polarization data, water and non-water bodies' overlapping area is smaller and more separable, which is more suitable for extracting water. Therefore, this paper uses VH cross-polarization band to extract water information of GF-3 SAR images. Due to the complexity of land covers, the interference of a large number of mountainous shadows, and the relatively small proportion of large-scale water bodies, it is not easy to obtain an effective water-land segmentation threshold through the statistical analysis of the global backscattering coefficient histogram. In this case, we selected the specific local areas, including Poyang lake and Caohu Lake. Then, the OSTU algorithm obtains the optimal threshold to extract the water and land in the study area, respectively. Concerning the backscattering differences between water bodies and land in specific areas in GF-3 images, the VH polarized backscattering coefficient is used to define the global threshold of water. Such method is already used for extracting the water from Sentinel-1 datasets [20,33].

Given the misidentification of water bodies caused by the low backscattering in the shadow area of the mountain, Shuttle Radar Topography Mission (SRTM) can be used to extract slope information to mask the non-water body areas. Theoretically, continuous stagnant water exists in areas with small slopes, while mountain shadows exist in large ones. Taking into account the slope characteristics of the flood detention area and the slope conditions of the shadow area formed by the GF-3 image incidence angle range $[27.18^\circ, 39.10^\circ]$, the slope threshold in this paper is set to be 8° . This threshold can effectively mask the shadow area of the mountain caused by SAR side-view imaging and retain the information of the flood detention area. Height above Nearest Drainage (HAND) [34] is a terrain index based on the drainage network. A previous study showed the advantages of using HAND maps for flood mapping to remove false positive surface water detection which are located high above the nearest drainage line [35]. In terms of employing the HAND model mask, the Yangtze River's middle and lower reaches receive abundant rainfall and dense water networks. The HAND threshold can be selected with an immense

value to reduce the leakage identification of flooded areas. Therefore, the HAND threshold is determined to be a shadow area of a flat area where the vertical distance between the mask and the nearest water is greater than 20 m.

For the GF-1/6, only RGB and NIR bands exist. The traditional method is to calculate the normalized difference water index (NDWI) [36]. However, ensuring the accuracy of water body information extraction is challenging due to shadows, dense vegetation, and impervious surface areas. To solve the challenge, Xu [21] proposed modified NDWI (MNDWI) based on green and SWIR bands. For challenging situations such as shade and dense vegetation, Chen et al. [37] suggested a method for extracting information about water bodies based on the tasseled cap transformation. Zhang and Crawford [38] developed a method using RGB bands to extract visible floodwater. To understand a feasible floodwater delineation technique, we measure the spectral features of both water and land cover categories in Figure 3. On GF-1/6 datasets, it was discovered that visible floodwater has a distinct spectral character (i.e., greater values of the green and blue bands). To this end, we develop a novel information spectral water index (WI), based on the differences between the values of RGB and NIR bands (B_g, B_r, B_b, B_{nir}):

$$WI = (B_g - B_r) * (B_b - B_{nir}) \quad (1)$$

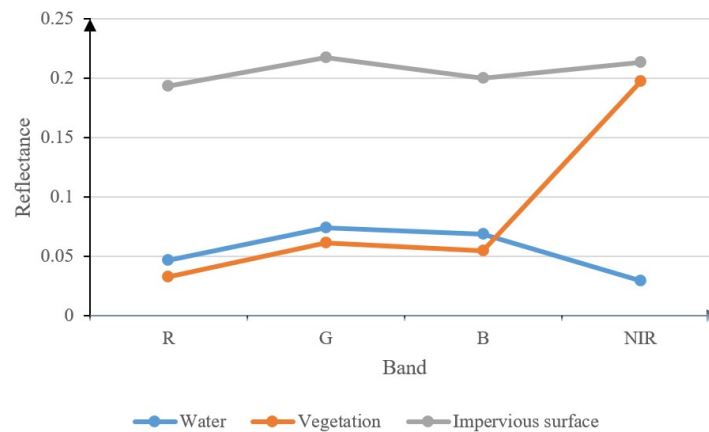


Figure 3. Spectral reflectance of Water, vegetation and impervious surface area in the study area of Dongting lake.

For the hyperspectral datasets, Xie et al. [39] developed a new hyperspectral difference water index to separate urban water bodies from the dark buildings and shadows using airborne hyperspectral images. Figure 4 shows the reflectance curves of water, vegetation, dark buildings, and bright buildings. The wavelength from band 1 to 32 is from 443 nm to 940 nm with the interval of 10 nm–20 nm. From band 17 to 32, the reflectance of water is lower than those of dark buildings and vegetation. The spectral curves of water suggest that the spectral shape and amplitude are suitable for classifying water for an entire image. Thus, we adopted the NDWI suitable for hyperspectral bands (NDWI_HIS) to extract the water:

$$NDWI_{HIS} = \frac{(\int_5^{10} R(b_i)d(b_i) - \int_{17}^{32} R(b_i)d(b_i))}{(\int_5^{10} R(b_i)d(b_i) + \int_{17}^{32} R(b_i)d(b_i))} \quad (2)$$

where b_i means the index of band in the hyperspectral images. $R(b_i)$ means the DN value of i th-band. Similar to the findings in [39], we manually set the threshold (0.2) to separate the water. The parts with values lower than the threshold are treated as water.

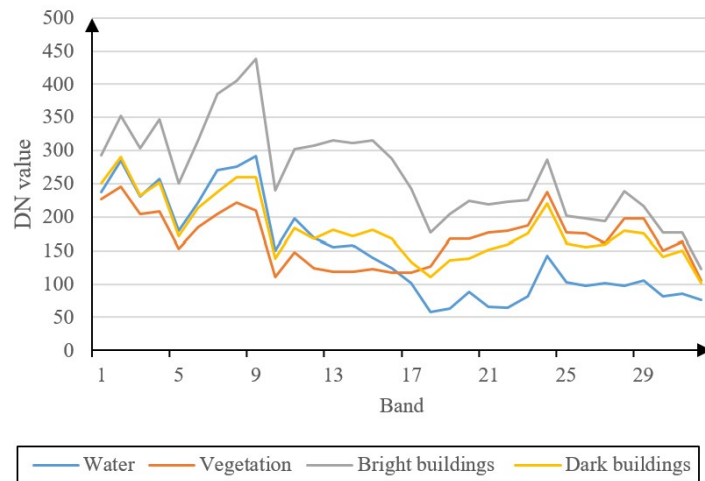


Figure 4. Spectral reflectance of Water, vegetation, dark and bright buildings of the HSI in the study area.

3.3. Fine Flood Extraction

The water results produced by the approaches as mentioned above contain varying degrees of noise, and the performance of flood between the difference of pre-disaster and post-disaster water is susceptible to massive label noise. In order to improve the performance, many methods [40] are proposed to solve the noisy-label setting. In this work, we adopt the T -revision [32], which learns the accurate labels from noisy labels by a transition matrix, to redefine the water results.

Let $\mathcal{X} \in \mathbb{R}^d$ be the feature space and $\mathcal{Y} = 1, 2, \dots, C$, where C is the number of classes. (X, Y) and (X, \hat{Y}) denote the true and noisy labels. In order to learn the transition matrices (T), the anchor points (i.e., the probability is equal to one or close to one of the true class) in the clean data domain is defined. Given an x , if the probability $P(Y = i|X = x) = 1$, for $k \neq i$, $P(Y = k|X = x) = 0$. Then, T can be obtained via estimating the noisy class probabilities for anchor points:

$$T_{ij} = P(\hat{Y} = j|X = x) = \sum_{k=1}^C T_{kj}P(Y = k|X = x) \quad (3)$$

The main flowchart, which is shown in Figure 5, include the following steps:

1. input the noisy label datasets to the neural network to learn the probability $P(\hat{Y}|X)$ by minimizing the unweighted loss without a noise adaption layer.
2. initialize T (Equation (3)) by using the samples with the highest learned probabilities.
3. in order to further exploit the true transition matrix T , a slack variable ΔT is added to the initialization T .
4. learn the neural network with T by minimizing the weighted loss.

The water extraction results of pre-flood and post-flood are redefined using the T -revision, and the final flood is derived from the difference of redefined water results of pre-flood and post-flood.

For the T -revision method, we followed the setting in [32], the SGD with momentum 0.9, weight decay 10^{-4} and an initial rate of 10^{-2} is used to estimate the translation matrix. In the revision part, we use the same settings as the previous one. Then, the learning rate is divided by ten after the 40th epoch and 80th epoch, and the total epoch is 100. Then, the optimizer and learning rate is switched to Adam and 5×10^{-7} to fine-tuning T and a slack variable ΔT . The batch size is set to be 16, and only horizontal random flips are used for the data argumentation. It should be emphasized that the number of bands used for GF-3 SAR, GF-1/6 multispectral, and Zhuhai-1 hyperspectral is 2, 4, and 32, respectively.

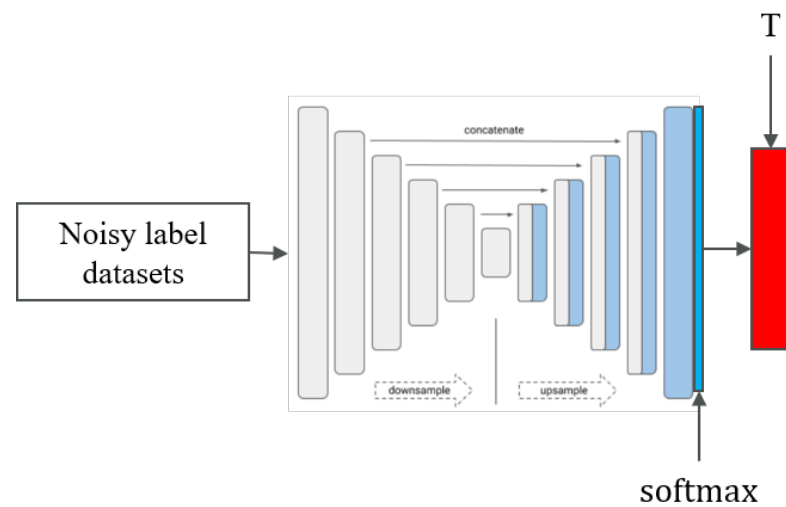


Figure 5. The main flowchart of T-revision.

4. Experimental Results and Analysis

4.1. Coarse Water Extraction

Figure 6 has shown the GF-3 SAR VH band and statistics of DN values in Poyang Lake and Chao Lake. This figure shows that the optimal threshold to separate water and non-water derived from OSTU methods is 130 and 134, respectively. Regarding the DN values difference between water bodies and land in GF-3 images, the optimal global threshold of the VH band is 130. Then, the coarse water is extracted based on the combination of optimal global threshold, slope, and HAND threshold.

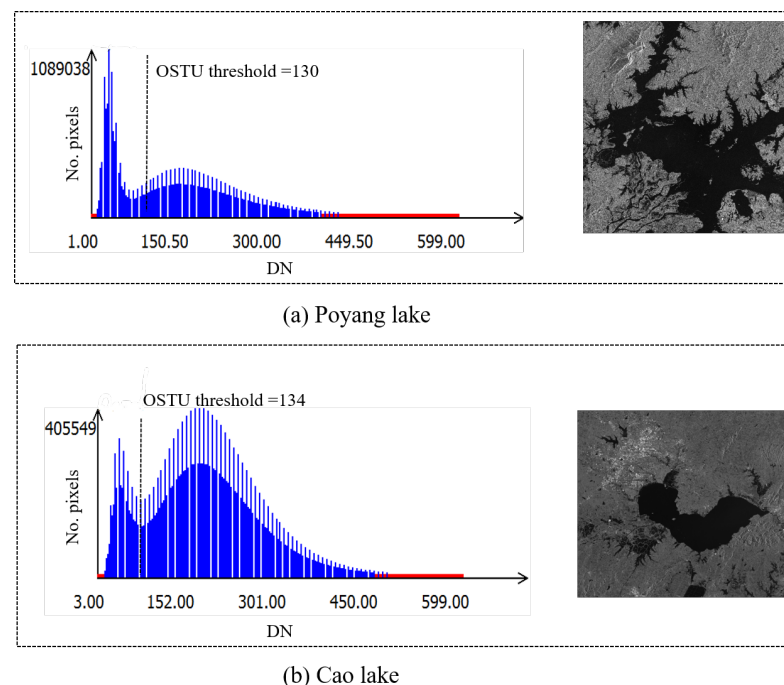


Figure 6. The GF-3 SAR HV band and statistics of DN values in Poyang Lake and Chao Lake.

Figure 7 has shown the water indexes and their statistics of GF-1 multispectral and Zhuhai hyperspectral datasets. This figure shows that using the optimal value of 0 is easy to separate the water and non-water in GF-1 datasets. However, the optimal value of hyperspectral is not straightforward to find. We manually set the threshold to -0.1 .

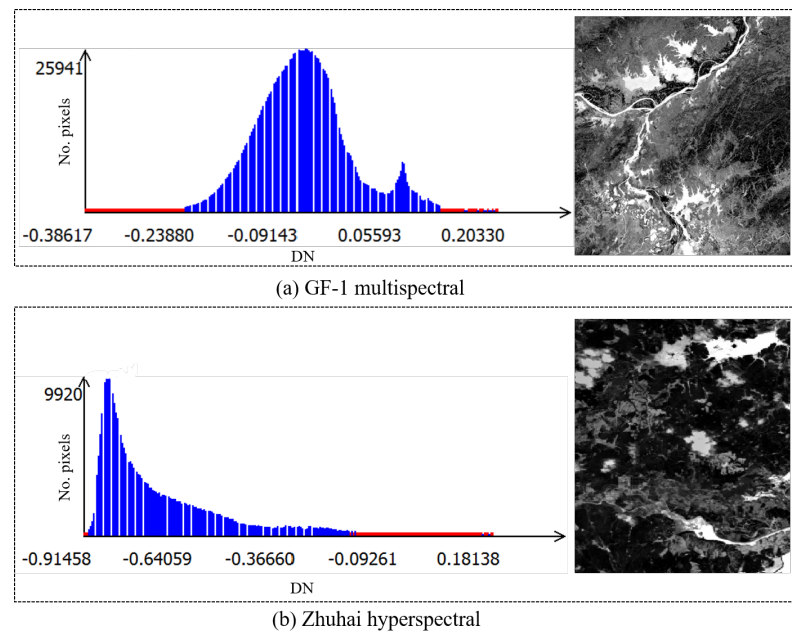


Figure 7. The statistics of WI values of GF-1 and Zhuhai-1 hyperspectral datasets.

Figures 8–10 have shown the coarse water results of GF-3 SAR, GF-1 multispectral and Zhuhai-1 hyperspectral datasets using the above-mentioned methods. From the figures, the method successfully extracts the main water body areas (with the overall accuracies over 80%). However, speckle noise and thin clouds fail to delete the majority of the erroneous information in all circumstances. Some regions were categorized as water, possible dark things, or asphalt when looking at building locations. Many of the incorrect parts were classified as shadows on the mountains. In the following, we introduce deep learning with noisy-label learning to remove such noise parts.

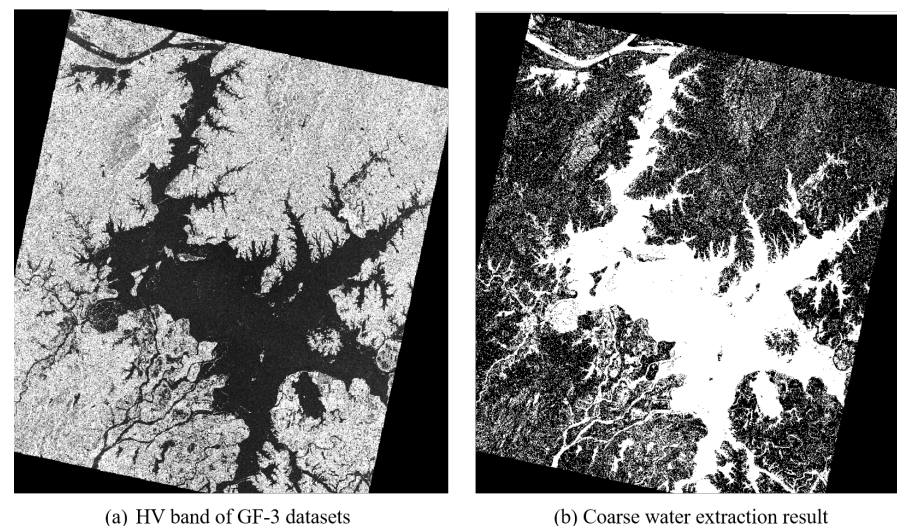


Figure 8. Coarse water extraction of GF-3 SAR.

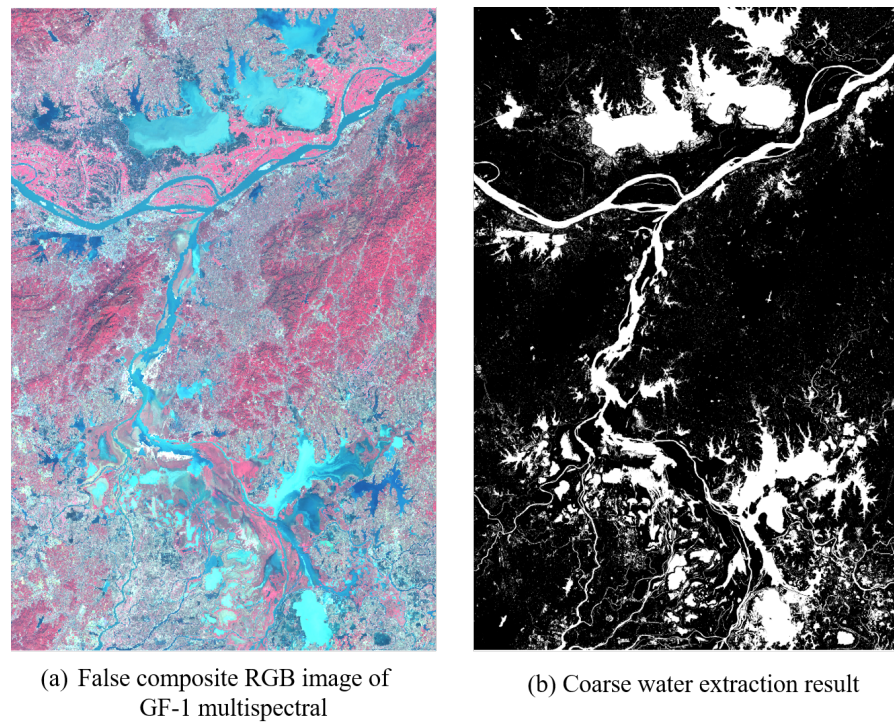


Figure 9. Coarse water extraction of GF-1 multispectral.

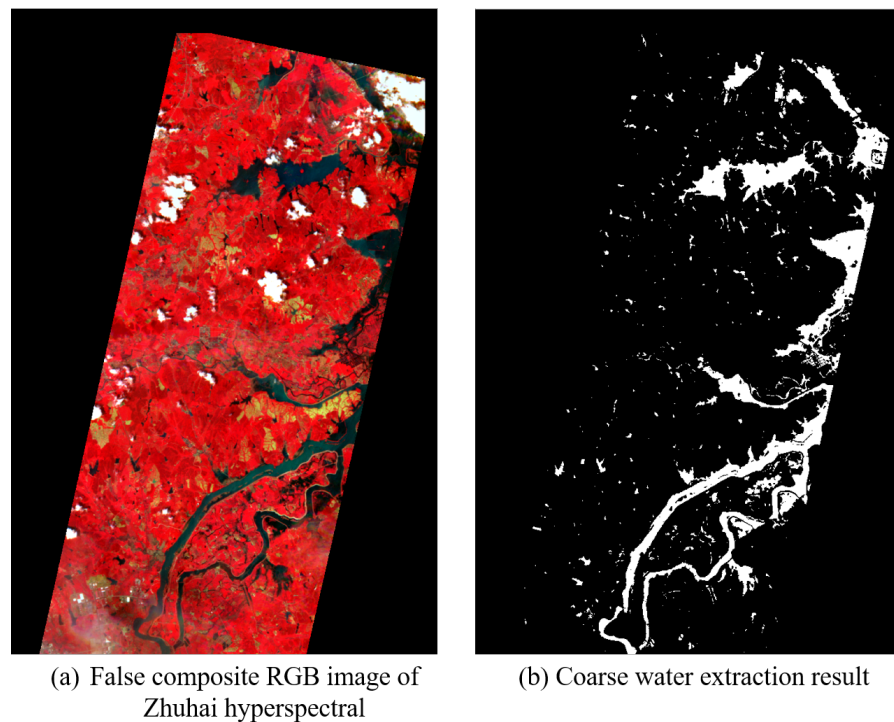


Figure 10. Coarse water extraction of Zhuhai-1 hyperspectral.

4.2. Fine Water Extraction and Accuracy Evaluation

For all the datasets, we cut the images into multiple patches with the size of 256×256 and 32×32 for SAR/multispectral and hyperspectral, respectively. For the semantic segmentation network, we use the U-net with the encoder of Efficient-B0 by considering the performance and computational complexity (https://github.com/qubvel/segmentation_models.pytorch (accessed on 1 October 2020)).

Five hundred samples were selected from the study area with, respectively, low, medium, and high water densities, to evaluate the accuracy of the water extraction results. The overall accuracy (OA) and Kappa coefficients are used as the measures (seen the results in Table 3). From this table, the fine results significantly improved the extraction performance. Taking the GF-1 MSI image as an example, the OA and Kappa of the coarse result are 82.45% and 78.67%. The fine result with Unet improved the two measures to 86.95% and 82.41%. With the support of the powerful capability of T-revision, the results were finally achieved at 94.27% and 91.72%, respectively.

Table 3. OA and kappa (%) of fine water extraction results.

Methods	GF-1 MSI	GF-3 SAR	Zhuhai-1 HSI
Coarse results	82.45 (78.67)	83.56 (81.54)	85.21 (81.79)
Fine results with Unet	86.95 (82.41)	91.37 (89.64)	89.18 (85.33)
Fine results with Unet and T-revision	94.27 (91.72)	95.74 (92.16)	93.24 (91.72)

Figures 11–13 show the fine water extraction results from the Unet with or without T-revision. Unexpectedly, the categorization using Unet produced the best results in the accuracy analysis and revealed no misleading information. Despite this, several minor water objects and rivers were not detected as water. When we include the T-revision to redefine the water, such rivers, small water objects, and the boundary of large water areas are maintained.

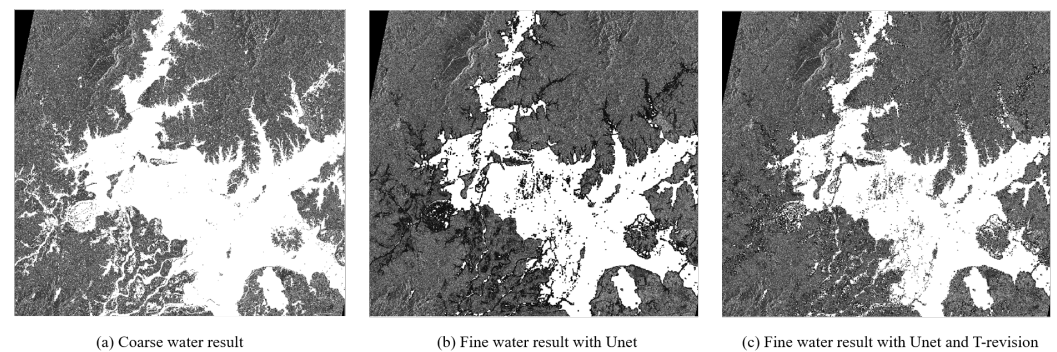


Figure 11. Fine water extraction of GF-3 SAR datasets.

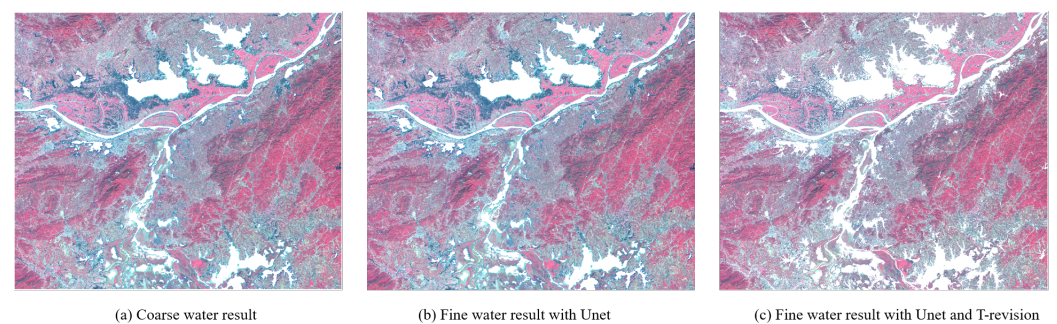


Figure 12. Fine water extraction of GF-1 multispectral.

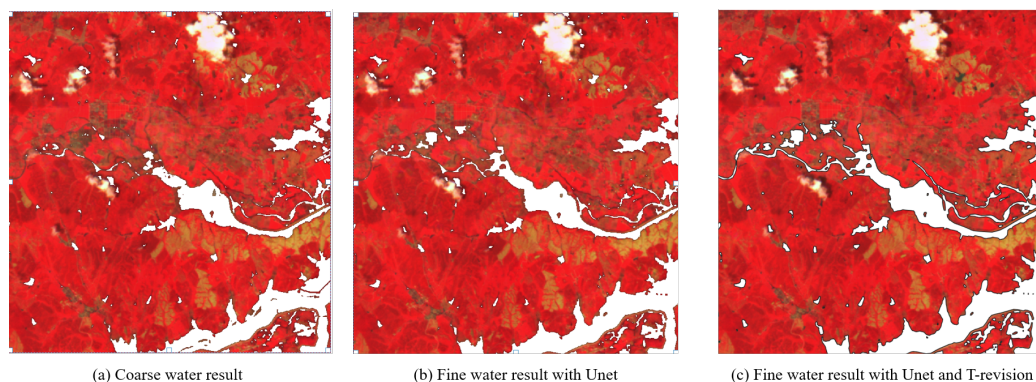


Figure 13. Fine water extraction of Zhuhai hyperspectral.

4.3. Flood Detection

In this section, we selected two pairs to show the flood mapping areas in the study area. The first one (seen in Figure 14), which is mainly located at the Poyang lake, includes the pre-flood with GF-1 (acquired on 2020-2-18) and the post-flood with GF-3 (acquired on 2020-7-11). The latter one (seen in Figure 15), which is located in the rural area of Jiangxi province, is the pre-flood with hyperspectral (acquired at 2020-3-15) and the post-flood hyperspectral (acquired at 2020-7-17) datasets.

As can be shown in Figure 14, the main change area is the boundary of Poyang Lake, which is caused by the heavy rain during the summer season. The results in Figure 15 indicated that the flood area includes the boundary in the river, the farmland and causes the collapse of the built-up areas. It should be noted that our proposed framework is suitable for different source images to extract the water and flood in an effective way. In this case, we can provide the rapid damage mapping in 2–3 h with multi source datasets when the flood disaster happens. If time-series datasets are provided, our proposed framework can also provide the trend of flood during the period of disaster, which may useful for the flood warning. Furthermore, such framework can be easily extended to the other disasters.

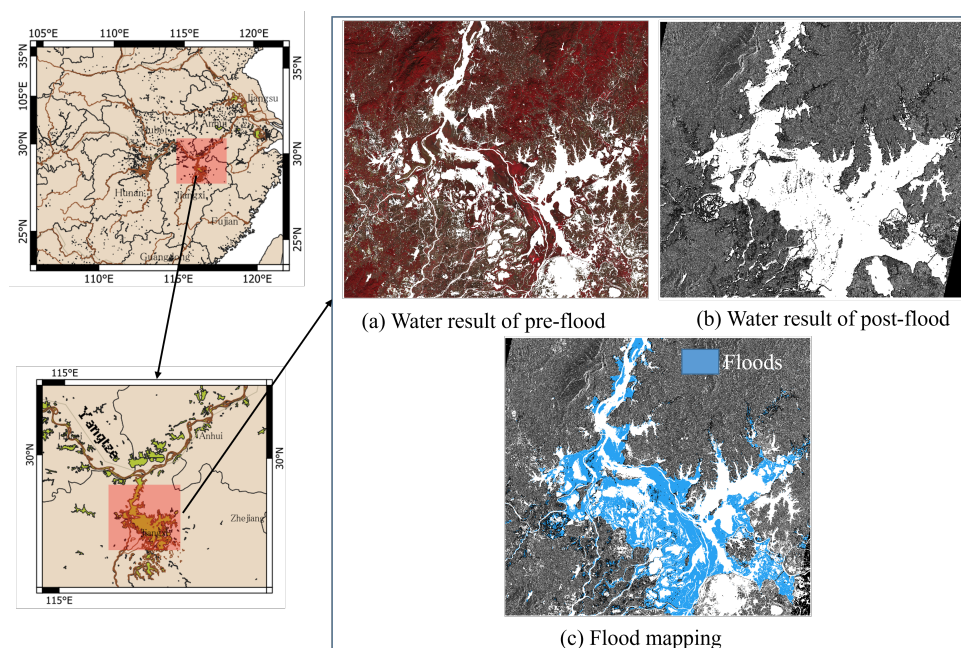


Figure 14. Flood mapping based on the pre-flood GF-1 multispectral and post-flood GF-3 SAR datasets.

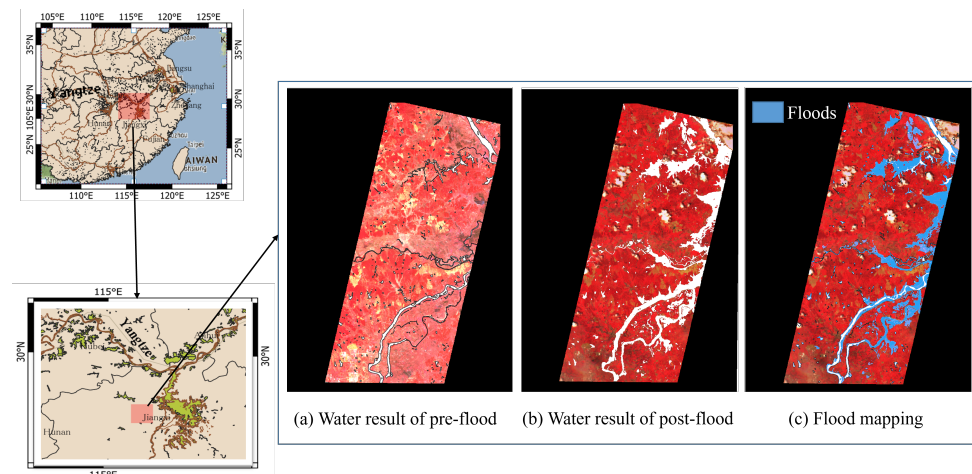


Figure 15. Flood mapping based on the pre- and post-flood Zhuhai-1 hyperspectral datasets.

5. Conclusions

In order to make an emergency response of flood mapping in a large area, this work introduced the new flood mapping flowchart based on the multi-source Chinese satellite datasets. The main conclusions and contributions are summarized as follows:

1. For different source images, we design different methods to extract the coarse water bodies. For instance, we introduce an effective binarization segmentation (OSTU) for SAR images. For multispectral and hyperspectral datasets, we define the different water indexes to extract the water bodies.
2. To improve the results, we introduced the noisy label learning to remove the noise and redefine the misclassified water bodies from the previous coarse methods. More specifically, the T-revision method is adopted and slightly improves the extraction results.

Author Contributions: Conceptualization, L.Z.; Data curation, L.Z. and J.X.; Formal analysis, L.Z. and J.X.; Funding acquisition, L.Z. and J.X.; Investigation, L.Z. and J.X.; Methodology, L.Z. and J.X.; Project administration, L.Z.; Resources, L.Z.; Software, L.Z.; Supervision, L.Z.; Validation, L.Z.; Visualization, L.Z.; Writing—original draft, L.Z.; Writing—review & editing, L.Z. All authors have read and agreed to the published version of the manuscript.

Funding: This work was supported by Special Research Assistant Project of CAS, KAKENHI Grant Number 19K20309JSPS Bilateral Joint Research Project (Grant number JPJSBP 120203211), and the Open Research Fund of National Earth Observation Data Center (Grant number NODAOP2020021).

Institutional Review Board Statement: Not applicable.

Informed Consent Statement: Not applicable.

Acknowledgments: The authors would like to thank the ChinaGEOSS Data Sharing Network, China National Space Administration (CNSA) and Zhuhai Obita Aerospace Technology Co., Ltd., for providing the Gaofen and hyperspectral datasets, respectively. The authors would also like to thank Piesat Information Technology Co., Ltd. to provide the software.

Conflicts of Interest: The authors declare no conflict of interest.

References

1. Tralli, D.; Blom, R.; Zlotnicki, V.; Donnellan, A.; Evans, D. Satellite remote sensing of earthquake, volcano, flood, landslide and coastal inundation hazards. *ISPRS J. Photogramm. Remote Sens.* **2005**, *59*, 185–198. [[CrossRef](#)]
2. Schumann, G.J.P.; Brakenridge, G.R.; Kettner, A.J.; Kashif, R.; Niebuhr, E. Assisting Flood Disaster Response with Earth Observation Data and Products: A Critical Assessment. *Remote Sens.* **2018**, *10*, 1230. [[CrossRef](#)]
3. Zanardo, S.; Nicotina, L.; Hilberts, A.G.J.; Jewson, S.P. Modulation of Economic Losses From European Floods by the North Atlantic Oscillation. *Geophys. Res. Lett.* **2019**, *46*, 2563–2572. [[CrossRef](#)]
4. Clift, P.D.; Holbourn, A.; France-Lanord, C.; Zheng, H. Evolution of the Asian Monsoon, *Eos*, 101. Published on 25 June 2020. Available online: <https://eos.org/science-updates/evolution-of-the-asian-monsoon> (accessed on 23 July 2021).

5. Excessive Monsoon Rains Flood Asia. Available online: <https://earthobservatory.nasa.gov/images/147006/excessive-monsoon-rains-flood-asia> (accessed on 30 November 2020).
6. The Ministry of Emergency Management Announces the National Ten Natural Disasters in 2020. Available online: <http://www.chinanews.com/gn/2021/01-02/9377255.shtml> (accessed on 10 January 2020).
7. Adriano, B.; Xia, J.; Baier, G.; Yokoya, N.; Koshimura, S. Multi-Source Data Fusion Based on Ensemble Learning for Rapid Building Damage Mapping during the 2018 Sulawesi Earthquake and Tsunami in Palu, Indonesia. *Remote Sens.* **2019**, *11*, 886. [[CrossRef](#)]
8. Brunner, D.; Lemoine, G.; Bruzzone, L. Earthquake Damage Assessment of Buildings Using VHR Optical and SAR Imagery. *IEEE Trans. Geosci. Remote Sens.* **2010**, *48*, 2403–2420. [[CrossRef](#)]
9. Gianinetto, M.; Villa, P.; Lechi, G. Postflood damage evaluation using Landsat TM and ETM+ data integrated with DEM. *IEEE Trans. Geosci. Remote Sens.* **2006**, *44*, 236–243. [[CrossRef](#)]
10. Goffi, A.; Stroppiana, D.; Brivio, P.A.; Bordogna, G.; Boschetti, M. Towards an automated approach to map flooded areas from Sentinel-2 MSI data and soft integration of water spectral features. *Int. J. Appl. Earth Obs. Geoinf.* **2020**, *84*, 101951. [[CrossRef](#)]
11. Xu, L.; Zhang, H.; Wang, C.; Fu, Q. Classification of Chinese GaoFen-3 fully-polarimetric SAR images: Initial results. In Proceedings of the 2017 Progress in Electromagnetics Research Symposium—Fall (PIERS—FALL), Singapore, 19–22 November 2017; pp. 700–705.
12. Li, D.; Wang, M.; Jiang, J. China’s high-resolution optical remote sensing satellites and their mapping applications. *Geo-Spat. Inf. Sci.* **2020**, *24*, 1–10. [[CrossRef](#)]
13. Serpico, S.B.; Dellepiane, S.G.; Boni, G.; Moser, G.; Angiati, E.; Rudari, R. Information Extraction From Remote Sensing Images for Flood Monitoring and Damage Evaluation. *Proc. IEEE* **2012**, *100*, 2946–2970. [[CrossRef](#)]
14. Wang, P.; Zhang, G.; Leung, H. Improving Super-Resolution Flood Inundation Mapping for Multispectral Remote Sensing Image by Supplying More Spectral Information. *IEEE Geosci. Remote Sens. Lett.* **2019**, *16*, 771–775. [[CrossRef](#)]
15. Notti, D.; Giordan, D.; Caló, F.; Pepe, A.; Zucca, F.; Galve, J.P. Potential and Limitations of Open Satellite Data for Flood Mapping. *Remote Sens.* **2018**, *10*, 1673. [[CrossRef](#)]
16. Giustarini, L.; Hostache, R.; Matgen, P.; Schumann, G.J.; Bates, P.D.; Mason, D.C. A Change Detection Approach to Flood Mapping in Urban Areas Using TerraSAR-X. *IEEE Trans. Geosci. Remote Sens.* **2013**, *51*, 2417–2430. [[CrossRef](#)]
17. Schlaffer, S.; Matgen, P.; Hollaus, M.; Wagner, W. Flood detection from multi-temporal SAR data using harmonic analysis and change detection. *Int. J. Appl. Earth Obs. Geoinf.* **2015**, *38*, 15–24. [[CrossRef](#)]
18. Huang, M.; Jin, S. Rapid Flood Mapping and Evaluation with a Supervised Classifier and Change Detection in Shouguang Using Sentinel-1 SAR and Sentinel-2 Optical Data. *Remote Sens.* **2020**, *12*, 2073. [[CrossRef](#)]
19. Cian, F.; Marconcini, M.; Ceccato, P. Normalized Difference Flood Index for rapid flood mapping: Taking advantage of EO big data. *Remote Sens. Environ.* **2018**, *209*, 712–730. [[CrossRef](#)]
20. DeVries, B.; Huang, C.; Armston, J.; Huang, W.; Jones, J.W.; Lang, M.W. Rapid and robust monitoring of flood events using Sentinel-1 and Landsat data on the Google Earth Engine. *Remote Sens. Environ.* **2020**, *240*, 111664. [[CrossRef](#)]
21. Xu, H. Modification of normalised difference water index (NDWI) to enhance open water features in remotely sensed imagery. *Int. J. Remote Sens.* **2006**, *27*, 3025–3033. [[CrossRef](#)]
22. Du, Y.; Zhang, Y.; Ling, F.; Wang, Q.; Li, W.; Li, X. Water Bodies’ Mapping from Sentinel-2 Imagery with Modified Normalized Difference Water Index at 10-m Spatial Resolution Produced by Sharpening the SWIR Band. *Remote Sens.* **2016**, *8*, 354. [[CrossRef](#)]
23. Mason, D.C.; Giustarini, L.; García-Pintado, J.; Cloke, H.L. Detection of flooded urban areas in high resolution Synthetic Aperture Radar images using double scattering. *Int. J. Appl. Earth Obs. Geoinf.* **2014**, *28*, 150–159. [[CrossRef](#)]
24. Zhu, X.X.; Tuia, D.; Mou, L.; Xia, G.; Zhang, L.; Xu, F.; Fraundorfer, F. Deep Learning in Remote Sensing: A Comprehensive Review and List of Resources. *IEEE Geosci. Remote Sens. Mag.* **2017**, *5*, 8–36. [[CrossRef](#)]
25. Yuan, Q.; Shen, H.; Li, T.; Li, Z.; Li, S.; Jiang, Y.; Xu, H.; Tan, W.; Yang, Q.; Wang, J.; et al. Deep learning in environmental remote sensing: Achievements and challenges. *Remote Sens. Environ.* **2020**, *241*, 111716. [[CrossRef](#)]
26. Cheng, G.; Xie, X.; Han, J.; Guo, L.; Xia, G.S. Remote Sensing Image Scene Classification Meets Deep Learning: Challenges, Methods, Benchmarks, and Opportunities. *IEEE J. Sel. Top. Appl. Earth Obs. Remote Sens.* **2020**, *13*, 3735–3756. [[CrossRef](#)]
27. Hashemi-Beni, L.; Gebrehiwot, A.A. Flood Extent Mapping: An Integrated Method Using Deep Learning and Region Growing Using UAV Optical Data. *IEEE J. Sel. Top. Appl. Earth Obs. Remote Sens.* **2021**, *14*, 2127–2135. [[CrossRef](#)]
28. Li, Y.; Martinis, S.; Wieland, M. Urban flood mapping with an active self-learning convolutional neural network based on TerraSAR-X intensity and interferometric coherence. *ISPRS J. Photogramm. Remote Sens.* **2019**, *152*, 178–191. [[CrossRef](#)]
29. Rahnmooonfar, M.; Murphy, R.; Miquel, M.V.; Dobbs, D.; Adams, A. Flooded Area Detection from Uav Images Based on Densely Connected Recurrent Neural Networks. In Proceedings of the IEEE International Geoscience and Remote Sensing Symposium, Valencia, Spain, 22–27 July 2018; pp. 1788–1791. [[CrossRef](#)]
30. Rudner, T.G.J.; Rufswurm, M.; Fil, J.; Pelich, R.; Bischke, B.; Kopacková, V.; Bilinski, P. Multi3Net: Segmenting Flooded Buildings via Fusion of Multiresolution, Multisensor, and Multitemporal Satellite Imagery. In Proceedings of the AAAI Conference on Artificial Intelligence, Honolulu, HI, USA, 27 January–1 February 2019; pp. 702–709.
31. Bonafilia, D.; Tellman, B.; Anderson, T.; Issenberg, E. Sen1Floods11: A georeferenced dataset to train and test deep learning flood algorithms for Sentinel-1. In Proceedings of the IEEE/CVF Conference on Computer Vision and Pattern Recognition (CVPR) Workshops, Seattle, WA, USA, 13–19 June 2020; pp. 835–845.

32. Xia, X.; Liu, T.; Wang, N.; Han, B.; Gong, C.; Niu, G.; Sugiyama, M. Are Anchor Points Really Indispensable in Label-Noise Learning? In Proceedings of the Advances in Neural Information Processing Systems, Vancouver, BC, Canada, 8–14 December 2019, pp. 6835–6846.
33. Li, Y.; Niu, Z.; Xu, Z.; Yan, X. Construction of High Spatial-Temporal Water Body Dataset in China Based on Sentinel-1 Archives and GEE. *Remote Sens.* **2020**, *12*, 2413. [[CrossRef](#)]
34. Nobre, A.; Cuartas, L.; Hodnett, M.; Rennó, C.; Rodrigues, G.; Silveira, A.; Waterloo, M.; Saleska, S. Height above the Nearest Drainage—A hydrologically relevant new terrain model. *J. Hydrol.* **2011**, *404*, 13–29. [[CrossRef](#)]
35. Bioresita, F.; Puissant, A.; Stumpf, A.; Malet, J.P. A Method for Automatic and Rapid Mapping of Water Surfaces from Sentinel-1 Imagery. *Remote Sens.* **2018**, *10*, 217. [[CrossRef](#)]
36. McFEETERS, S.K. The use of the Normalized Difference Water Index (NDWI) in the delineation of open water features. *Int. J. Remote Sens.* **1996**, *17*, 1425–1432. [[CrossRef](#)]
37. Chen, C.; Wang, L.; Chu, Y.; He, X. The method for water body information extraction in complex environment using GF-1 WFV images. In *E3S Web of Conferences*; EDP Sciences: Les Ulis, France, 2020; Volume 213, p. 03024. [[CrossRef](#)]
38. Zhang, Y.; Crawford, P. Automated Extraction of Visible Floodwater in Dense Urban Areas from RGB Aerial Photos. *Remote Sens.* **2020**, *12*, 2198. [[CrossRef](#)]
39. Xie, H.; Luo, X.; Xu, X.; Tong, X.; Jin, Y.; Pan, H.; Zhou, B. New hyperspectral difference water index for the extraction of urban water bodies by the use of airborne hyperspectral images. *J. Appl. Remote Sens.* **2014**, *8*, 085098. [[CrossRef](#)]
40. Song, H.; Kim, M.; Park, D.; Lee, J.G. Learning from Noisy Labels with Deep Neural Networks: A Survey. *arXiv* **2020**, arXiv:cs.LG/2007.08199.